Electronic Supplementary Material (ESI) for Journal of Materials Chemistry A.

Supporting Information to

Spontaneous Energy Generation at the Air-Hydrogel Interface with Ultrahigh Ion Activity

Shanshan Liu[a], Rongjie Yang[a], Tao Yang[b], Zisheng Luo[b], Bin Su*[a] & Xingyu Lin*[b, c]

*Corresponding author. Email: subin@zju.edu.cn (B. S.); xingyu@zju.edu.cn (X. L.)

Table of Contents

S1. Methods

Preparation of AIEG device

The ionic hydrogel was synthesized by thermal polymerization. Acrylic acid aqueous solution (5 mol/L, 99%, Macklin) was neutralized by KOH (95%, Macklin), followed by the addition of ammonium persulfate (0.02 mol/L, 98%, J&K) and N, N'-methylene bisacrylamide (0.026 mol/L, 99%, Aladdin). The mixture was then polymerized at 60 °C for 5 h. All aqueous solutions were prepared with ultrapure water (18.2 MΩ) unless otherwise stated. All chemicals were used as received without further purification unless otherwise noted.

The gold electrode was fabricated by sputtering a thin layer of Ti (20 nm) as adhesive layer on the glass substrate and a 100 nm thick Au layer as the conducting layer using magnetron sputtering technology. An AIEG device involves the sandwiching of ionic hydrogel with different thicknesses between two gold electrodes.

Electrical measurements

The electrical measurements were conducted under ambient conditions, unless otherwise stated. The temperature and RH during the measurement were controlled at 19-25 °C and 50-60%, respectively, except for the experiment with varied RH. The voltage was recorded with an Autolab electrochemical workstation. The *I-V* curve was measured by a Keithley picoammeter (Keithley Instruments, Cleveland, 6487). The heater (Ao Sheng Instruments, MiniT-C) was used for heating the hydrogel. The temperature recorder (THMA temperature recorder, Wenkong Instruments) and

temperature microsensor (Tenghui Wenkong Instruments, PT100) were used to measure the temperature in real-time.

Characterization

The morphology and elemental distribution of hydrogel samples were characterized by scanning electron microscope (SEM, Hitachi, SU8010) with EDS mapping. Samples were treated with vacuum freeze-drying before SEM. Fourier transform infrared spectrometer (FTIR, Thermo scientific, Nicolet iS10) spectra were used for characterizing functional groups of hydrogel using the KBr pellet method. Raman spectra were recorded with a LabRAM HR Raman spectrometer (Horiba France SAS, labRam Soieil), which possesses automatic movement control function in the vertical direction. The mechanical properties of the hydrogels were measured by an electronic universal testing machine (UTM2102, SUNS technology stock Co., Ltd., Shenzhen, China). The test was carried out under the condition that the gauge distance was 20 mm and the loading speed was 5 mm/min.

S2. Measurement of cation selectivity(t_+)

As shown in **Supplementary Fig. 1a**, the ionic hydrogel was prepared in a U-shaped glass tube, then each side was filled with 1 mM KCl solution. After balancing for 24 h, the solution on one side was heated while the other did not. The voltage with temperature difference variation was simultaneously measured (**Supplementary Fig. 1b**). A micro-ceramic heater (Zhuhai Huiyou Electronics) connected to a DC power (QJ6003S, Ningbo Jiuyuan Electronics) was used to heat the solution. The voltage was recorded with an Autolab electrochemical workstation (PGSTAT302N, Metrohm) using a pair of Ag/AgCl electrodes.

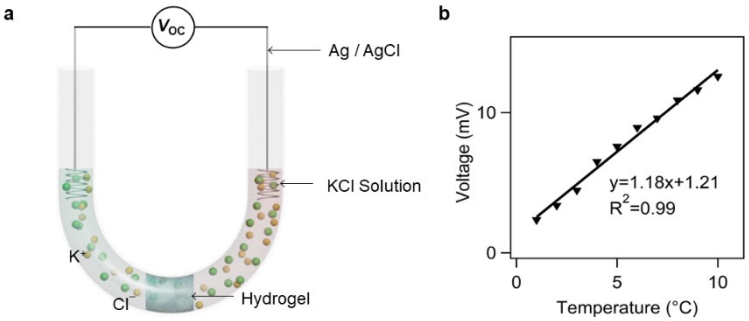

Supplementary Figure 1. a The U-tube device and a pair of Ag/AgCl electrodes for measuring the ion selectivity of the ionic hydrogel. **b** The variation of voltage (measured as the open circuit potential) with temperature difference.

The voltage between two electrodes (termed E) can be calculated by the following equation,[1]

$$E = -2t_+ \frac{R}{T} \Delta T \ln c \tag{S1}$$

According to this equation and the slope of line in **Supplementary Fig. 1b**, t_+ was calculated to be 0.99.

S3. Fourier transform infrared (FTIR) spectra

FTIR Spectra of the ionic hydrogel shows two signature bands at 3380 cm^{-1} (O–H stretching vibration) and 1600 cm^{-1} (C=O stretching vibration).[2] The functional groups did not change before and after power output.

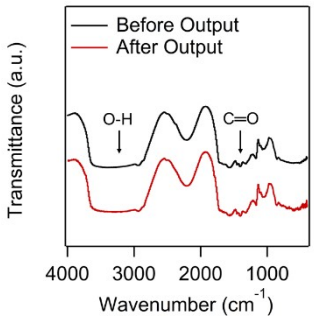

Supplementary Figure 2. FTIR spectra of ionic hydrogel before (black curve) and after (red curve) continuous power output.

S4. Light effect on the voltage output

The continuous voltage output for 24 h under daylight and dark proves that light has little effect on the voltage output.

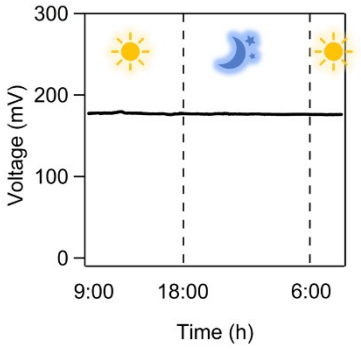

Supplementary Figure 3. The continuous voltage output of AIEG under an ambient condition for 24 h.

S5. The effect of electrode materials

The effect of electrode materials was studied by measuring the voltage output with indium tin oxide (ITO) and carbon electrodes.

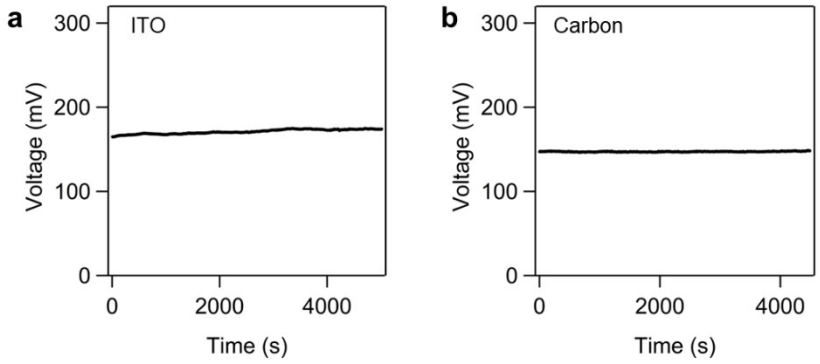

Supplementary Figure 4. **a**, **b** Voltage output of AIEG devices using ITO (**a**) and carbon (**b**) as electrodes under an ambient environment.

S6. The effect of electrolytes

Because the saturated vapor pressure varies with different electrolyte solutions,[3] the effect of electrolytes was studied.

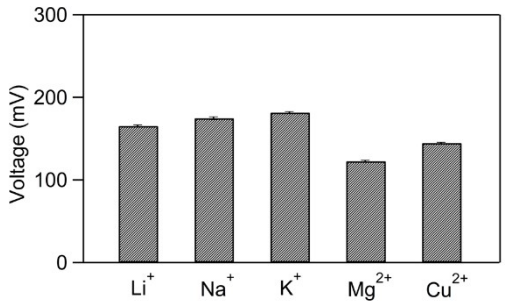

Supplementary Figure 5. Voltage output of AIEG devices measured with different electrolytes.

S7. The weight loss of hydrogel

Once the ionic hydrogel was moved out of the electrolyte solution, water evaporation at the air-hydrogel interface occurred and obvious loss of weight was observed. For hydrogel with different thicknesses, the weight changes per unit area are the same, indicating water evaporation occurs only in a thin layer on the top of the hydrogel.

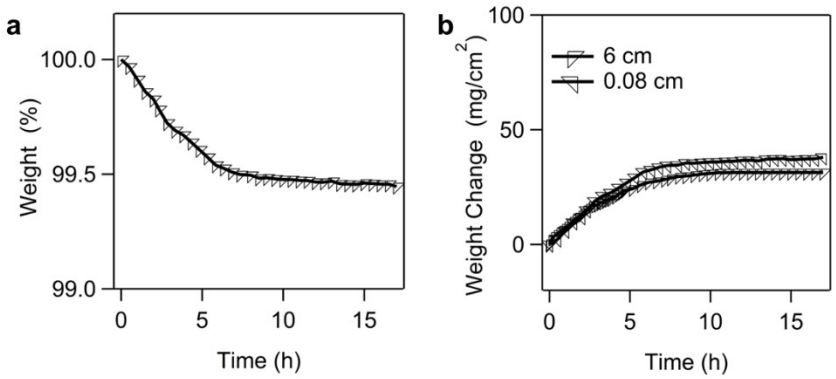

Supplementary Figure 6. a The weight change of AIEG (thickness: 6 cm). **b** Normalized weight change of AIEG with different thicknesses (800 μm, 6 cm).

S8. Raman spectrum

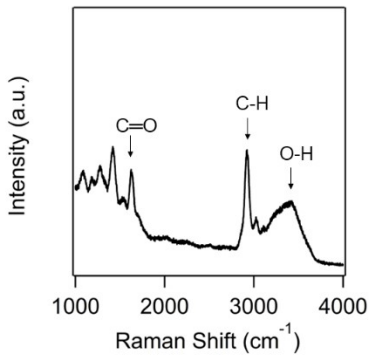

Supplementary Figure 7. Raman spectrum of the ionic hydrogel.

S9. Element mapping images

The energy dispersive spectra (EDS) of K^+ measured along the vertical direction of the hydrogel can reveal the distribution of the ions. **Supplementary Fig. 8** shows that K^+ accumulates at the air-gel interface.

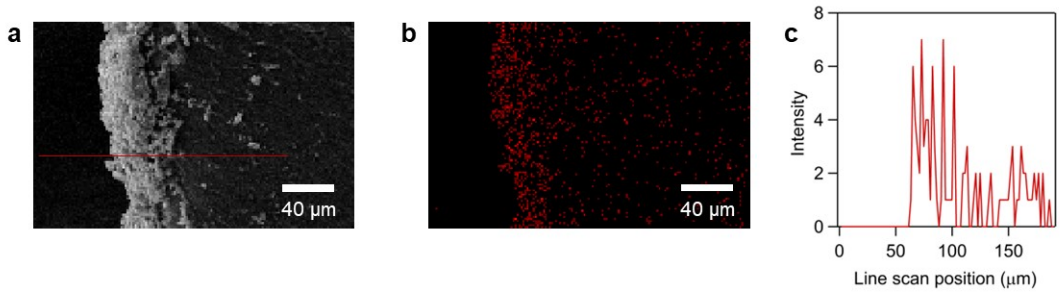

Supplementary Figure 8. The spatial distribution of K^+ in the vertical direction of hydrogel after water evaporation. **a** SEM side view of the hydrogel. **b** Element mapping image of energy dispersive spectra of K^+ at the air-hydrogel interface. **c** Spatial distribution of K^+ along the marked red line in **a**.

S10. *In-situ* measurement of the concentration of Cl^-

The measurement was conducted using a two-electrode system, in which an Ag/AgCl wire and an Ag/AgCl (saturated KCl) acted as the indicator and reference electrode, respectively. In principle, the potential of the reference electrode does not vary with the solution composition, while that of the indicator electrode changes with the activity of Cl^-. Thus, the open circuit potential measured by two electrodes (E_{Cl^-}) reflects the localized concentration of Cl^- (c') in terms of the Nernst equation,

$$E_{Cl^-} = \frac{RT}{zF} \ln \frac{3.4}{c'} \quad \text{(S2)}$$

The two-electrode system was firstly used to measure Cl^- in solutions containing different concentrations of KCl, as shown in **Supplementary Fig. 9a**.

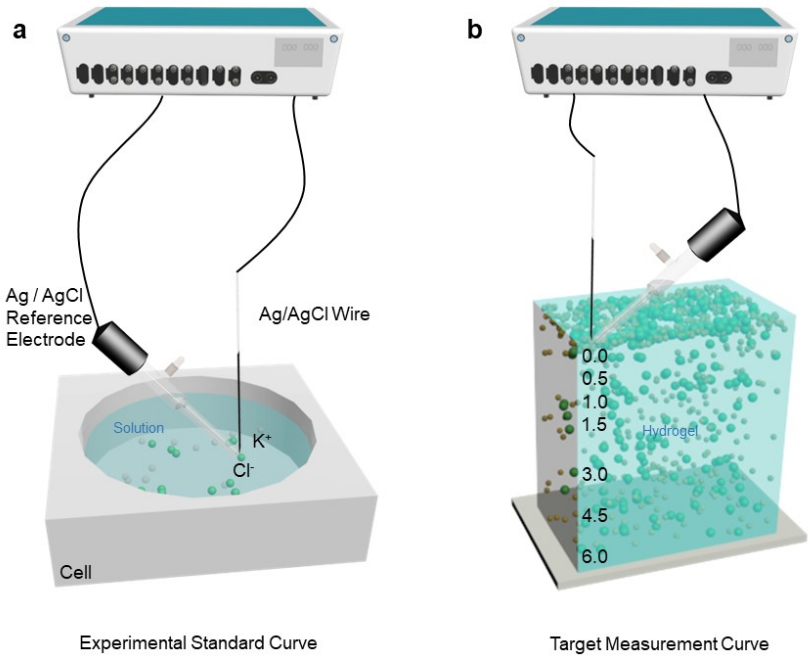

Supplementary Figure 9. a and **b** The measurement of the concentration of Cl^- using a two-electrode system in solutions containing different concentrations of KCl (**a**) and hydrogel at different heights containing 1mM KCl (**b**).

The experimental calibration curve, namely the measured potential against the concentration of Cl^-, matches the theoretical prediction of equation S2 well (**Fig. 3e**).

Based on the same principle, the two-electrode system was used for *in-situ* measurement of the concentration of Cl^- in hydrogel. To eliminate the build-in potential inside the hydrogel, these two electrodes were positioned close to each other. The measured potential at different depths were employed to calculate the localized concentration of Cl^- using equation S2.

The concentration of Cl^- at different heights (c_h) in the bulk hydrogel is low and relatively stable, while the concentration of Cl^- at air-hydrogel interface (c_0) is much higher. And the logarithm trend line of c_0/c_h is consistent with the open-circuit voltage (V_{oc}) curve measured with two electrodes inserted at their-hydrogel interface (h = 0) and different heights of bulk hydrogel (h = 0.5, 1.0, 1.5, 3.0, 4.5, 6.0 cm) (**Supplementary Fig. 10**), respectively, suggesting that the voltage output links with the concentration ratio between interface and bulk hydrogel.

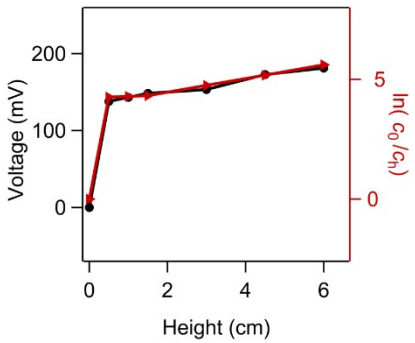

Supplementary Figure 10. The measured voltage output value at different heights of ionic hydrogel is consistent with the logarithm trend line of c_0/c_h.

S11. In-situ measurement of Cu^{2+} activity

Water in salt, that is, an aqueous electrolyte solution with ultra-high concentration, in which the hydration of salt imprisons a large number of water molecules in the electrolyte, and results in ultra-high activity coefficient of ions.[4] To determine the activity of Cu^{2+} in hydrogel and solution, a copper wire and an Ag/AgCl (at saturated KCl) were used as the indicator and reference electrodes, respectively, to measure the open circuit potential (E_{Cu}) in a solution containing different concentrations of Cu^{2+}. The redox equilibrium of Cu^{2+} at the surface of copper wire in $CuCl_2$ solution can be considered as,

$$Cu^{2+} + 2e^- \rightleftharpoons Cu \tag{S3}$$

E_{Cu} is given by the following Nernst equation,

$$E_{Cu} = E^{\ominus}_{Cu^{2+}/Cu} + \frac{RT}{zF}\ln(\gamma c_{Cu^{2+}}) - E_{Ag/AgCl} \tag{S4}$$

where $E_{Ag/AgCl}$ is fixed at a certain temperature. γ is the activity coefficient of Cu^{2+}. Assuming that the activity coefficient is 1 when the effective concentration (activity) is equal to the concentration, the activity coefficients of Cu^{2+} at different salt concentrations can be calculated by dividing the activity deduced from the experimental values with the known concentration according to equation S4. In the solution, the Cu^{2+} activity coefficient was calculated to be 24 based on the experimental data, as shown in **Fig. 3f**.

S12. Theoretical calculation

Due to the existence of carboxylic groups, the ionic hydrogel is negatively charged. So the movement of cations plays a leading role because of the cationic selectivity. Therefore, the open-circuit voltage can be measured between the top and bottom surfaces of hydrogel when a concentration difference is formed due to water evaporation at the air-hydrogel interface. Because the ion concentration on the top surface is larger, the bottom surface is the positive pole of open-circuit voltage. To quantitatively analyze the influence of environmental factors, such as wind power, humidity, and temperature on electricity output, we established a theoretical model. Considering the cross-linked skeleton structure obtained after vacuum freeze-drying (as revealed by the SEM image), the free volume of hydrogel is regarded as a porous structure.[5] To calculate the voltage output of AIEG, we consider the root cause of voltage is the electrolyte concentration gradient triggered by water evaporation at the air-hydrogel interface.

The driving force of water evaporation comes from the steam pressure difference (ΔP, Pa) between hydrogel surface and air,[6] which can be described by the following equation,

$$\Delta P = x_{H_2O} P_s - P_a \tag{S5}$$

where P_s is the saturated water vapor pressure (Pa) at the air-hydrogel interface, P_a partial pressure of water vapor (Pa) at the air-hydrogel interface and x_{H2O} the molar fraction of water in the hydrogel. Apparently, $\Delta P = 0$ refers to an equilibrium state, $\Delta P > 0$ drives the water evaporation and vice versa.

P_s can be straightforwardly calculated by Antoine's equation at a certain temperature,

$$\log_{10}\frac{P_s}{133.32} = 8.07 - \frac{1730.63}{T - 39.72} \tag{S6}$$

P_a is related to P_s via relative humidity (RH),

$$P_a = \mathrm{RH} \times P_s \tag{S7}$$

And x_{H2O} is given by the following equation S8,

$$x_{H_2O} = \frac{n_{H_2O}}{n_{total}} = \frac{n_{H_2O}}{n_{H_2O} + n_{K^+}} \tag{S8}$$

According to these equations, the water evaporation will finally stop at the equilibrium state when $x_{H2O} = \mathrm{RH}$. Thus, the voltage output of AIEG is obtained as,

$$V_{oc} = (2t_+ - 1)\frac{RT}{F}\ln\frac{c_1}{c_0} \tag{S9}$$

where c_1 is the concentration of K^+ at the hydrogel interface and can be calculated according to x_{H2O} (or RH) at the equilibrium state. c_0 is the concentration of K^+ in the bulk hydrogel, which is calculated to be 0.3 mol/L. Thus, equation S9 can be also rewritten as,

$$V_{oc} = (2t_+ - 1)\frac{RT}{F}\ln\frac{1 - \mathrm{RH}}{0.4(0.039 - 0.021\mathrm{RH})} \tag{S10}$$

Then the vapor phase thin-film model was used for simulating mass transfer. Water vapor concentration distributes unevenly in the layer of gas-phase film and depends on the water vapor diffusion coefficient and air flow under specific conditions.[7] When the wind speed (v, m/s) and viscosity (η, m^2/s) of air are considered, the vapor film is assumed to be a laminar boundary layer. In this layer, the fluid flows parallel to a certain

direction. And the flow layer is not mixed, that is, any exchange of mass or momentum only occurs between the adjacent layers. The mole flux of water vapor (J_{vapor}, mol/m^2/s) can be written as

$$J_{vapor} = -D_v \frac{dc}{dl} = \frac{D_v}{l}(c_i - c_a) \quad \text{(S11)}$$

where D_v is the diffusion coefficient of water vapor in air (m^2/s), l diffusion length (m). c_i and c_a are the concentration of water vapor at the hydrogel surface and in air, respectively,

$$c_i = \frac{x_{H_2O} P_s}{RT} \quad \text{(S12)}$$

$$c_a = \frac{P_a}{RT} = \frac{P_s \times RH}{RT} \quad \text{(S13)}$$

The diffusion length (l, m) is the thickness of vapor phase thin film, which can be described as,

$$l = \frac{\sqrt{A}}{0.646(\frac{v\sqrt{A}}{\eta})^{\frac{1}{2}}(\frac{\eta}{D_v})^{\frac{1}{3}}} \quad \text{(S14)}$$

where v and η are the air flow velocity (m/s) and viscosity (m^2/s), A surface area of the hydrogel. Thus, by introducing equations S12−14 into equation S11, J_{vapor} can be calculated as,

$$J_{vapor} = 0.646(x_{H_2O} - RH) \times \frac{P_s \cdot A^{-\frac{1}{4}} \cdot D_v^{\frac{2}{3}} \cdot \eta^{-\frac{1}{6}} \cdot v^{\frac{1}{2}}}{RT} \quad \text{(S15)}$$

According to equation S15, the water evaporation rate at the hydrogel surface will slow down with time, because x_{H2O} at the hydrogel surface gradually decreases, and finally stop when x_{H2O} approaches RH.

COMSOL simulations.

The commercial finite element software COMSOL Multiphysics (Version 5.2) is used for conducting numerical simulations. “Transport of Diluted Species” physical field is employed for simulating time-dependent and space-dependent transport of water and cation distribution at the air-hydrogel interface. As shown in the figure below, the evaporation process in air and diffusion process in the hydrogel is coupled and modelled as a 2D rigid frame. Boundary A is set as the evaporation surface, and the water flux direction is set accordingly. The diffusion coefficient (D_0) and the initial concentration of H_2O in the hydrogel are 2×10^{-12} m^2/s and 54.7 mol/L, respectively, as reported before. The temperature is 293.15 K.

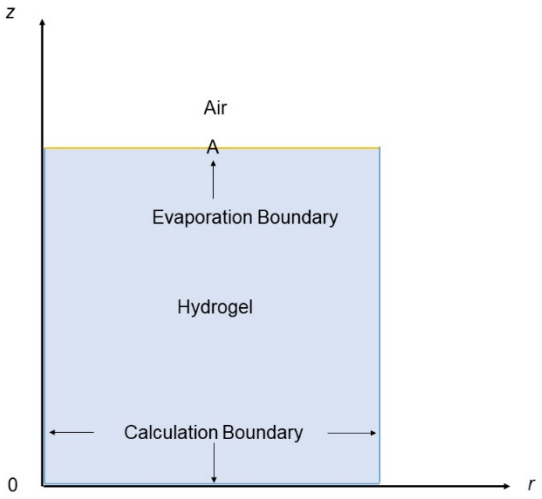

Supplementary Figure 11. 2D rigid frame employed in the COMSOL simulation (not the real scale). *r* and *z* are the coordinates in directions parallel and normal to the substrate surface, respectively.

In simulations, molecules in solution are transported exclusively by diffusion. So the transition conditions for all species follow the Fick’s second law,

$$\frac{\partial c_i}{\partial t} + \nabla J_i = R_i$$
$$J_i = -D_i \nabla c_i \quad \text{(S16)}$$

where c_i and D_i are the local concentration and diffusion coefficient of water molecules respectively. The above equation S16 can be used for simulating the diffusion of water molecules in the hydrogel. In addition to flux inside the hydrogel, J_{vapor} is the evaporation flux at the air-hydrogel interface, which can be calculated from equation S17 using parameters in Table S1,

$$J_{H_2O} = -0.00126\left(\frac{39c}{21c + 10^6} - 0.5\right) \quad \text{(S17)}$$

The main manuscript shows the simulation results in **Fig. 3g-i**.

Supplementary Table 1. Parameters used in COMSOL simulations

Molar fraction of water (x_{H_2O})	Diffusion Coefficient (D_v, m^2/s)	Area (A, m^2)	Wind speed (v, m/s)	Viscosity of air (η, m^2/s)	Molar mass of water ($M_{H_2O,}$ g/mol)
0.879	2×10^{-12}	10^{-4}	0.3	1.51×10^{-5}	18

S13. The effect of electrolyte concentration and pH

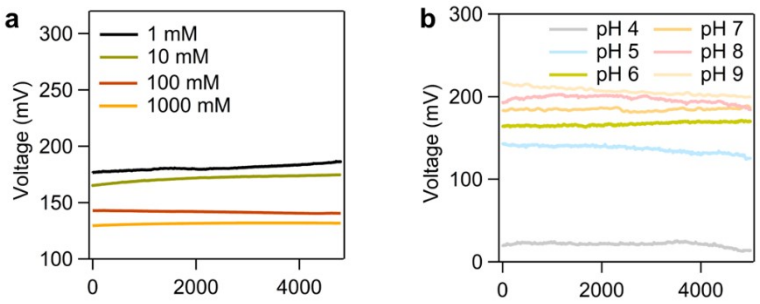

Supplementary Figure 12. **a** Voltage output of AIEG measured at different KCl electrolyte concentrations. **b** Voltage output of AIEG measured in solution with different pH.

S14. Theoretical calculation of the variation of output voltage with humidity

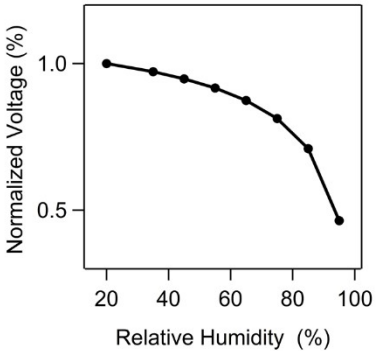

Supplementary Figure 13. Theoretical calculation of voltage output of AIEG at different RH (RH = 20%, Normalized Voltage = 1).

S15. The effect of temperature on power output

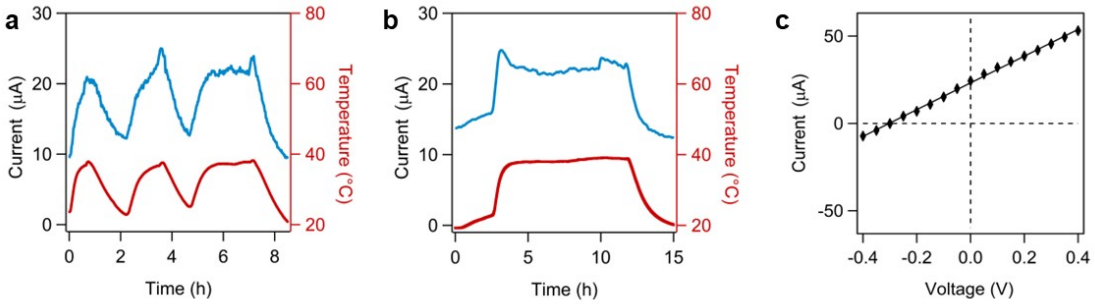

Supplementary Figure 14. The electric output performance of AIEG in the process of thermal and evaporation. **a** The current output of AIEG in the presence of additional heating-promoted evaporation. **b** Prolonged current output in response to heating. **c** Typical *I*–*V* curve in the presence of heating-promoted evaporation.

S16. Mechanical stability and flexibility

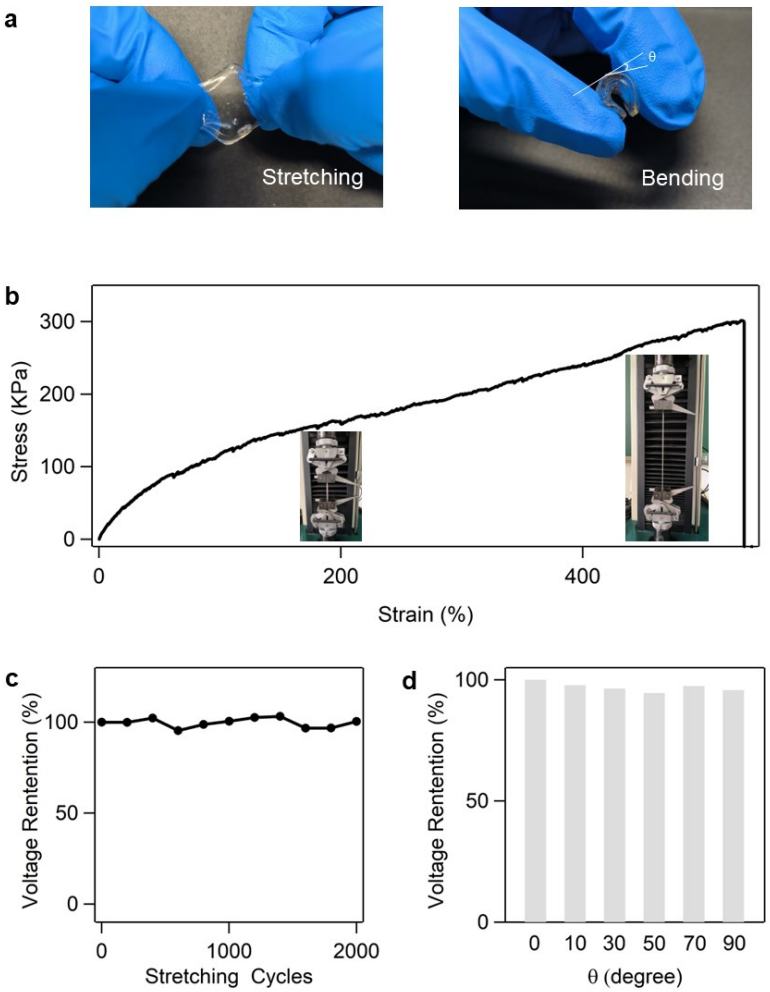

Supplementary Figure 15. The mechanical stability and flexibility of the hydrogel. **a** The photograph of deformability of the hydrogel. **b** Stress−strain curve of the hydrogel. **c** Voltage retention of the hydrogel after 2000 stretching cycles at a strain of 30%. **d** Voltage retention of the hydrogel under different bending angles.

References

1. K. Chen, L. Yao and B. Su, *J. Am. Chem. Soc.*, 2019, **141**, 8608-8615.
2. Q. Lyu, B. Peng, Z. Xie, S. Du, L. Zhang and J. Zhu, *ACS Appl. Mater. Interfaces*, 2020, **12**, 57373-57381.
3. I. G. Escalona, C. J. Gommes, N. Job, S. Blacher, C. G. Olivera-Fuentes, J.-P. Pirard and A. Léonard, *Microporous Mesoporous Mater.*, 2009, **117**, 61-66.
4. L. Suo, O. Borodin, T. Gao, M. Olguin, J. Ho, X. Fan, C. Luo, C. Wang and K. Xu, *Science*, 2015, **350**, 938-943.
5. Y. Xia, Q. Hou, H. Jubaer, Y. Li, Y. Kang, S. Yuan, H. Liu, M. W. Woo, L. Zhang, L. Gao, H. Wang and X. Zhang, *Energy Environ. Sci.*, 2019, **12**, 1840-1847.
6. E. Chiavazzo, M. Morciano, F. Viglino, M. Fasano and P. Asinari, *Nat. Sustain.*, 2018, **1**, 763-772.
7. R. Li, Y. Shi, M. Wu, S. Hong and P. Wang, *Nat. Sustain.*, 2020, **3**, 636-643.